electronics

Article

Defect and Fault Diagnosis Method for Three-Phase Cross-Bonded Cables Based on High-Frequency High-Voltage Coordinated Excitation

Zhongyuan Li [1], Xueting Wang [1], Zhen Zhang [1] and Ling Huang [2,*]

[1] Electric Power Research Institute, State Grid Heilongjiang Electric Power Co., Ltd., Harbin 150001, China
[2] National Key Laboratory of High-Efficiency Special Cable Technology, Harbin University of Science and Technology, Harbin 150080, China
* Correspondence: huangling@hrbust.edu.cn; Tel.: +86-19845727838

Abstract

To address severe transmission signal attenuation caused by inter-phase electromagnetic coupling in three-phase cross-bonded cables, which significantly limits the identification of insulation defects and fault types, this paper proposes a broadband impedance spectroscopy differential-frequency decoupling and defect diagnosis method based on three-phase high-frequency, high-voltage coordinated excitation. First, a decoupled transmission line model for three-phase cross-bonded cables is established to systematically analyze how the degree of insulation damage and fault equivalent impedance affect the frequency domain response at the test terminal. Three core diagnostic parameters, namely the fundamental resonant peak amplitude variation ratio, the resonant period change rate, and the initial phase offset, are extracted to construct a multi-dimensional collaborative diagnosis model for accurate defect and fault identification. Second, a high-voltage topology based on proportional optical isolation driving is designed to overcome the gain and bandwidth trade-off of conventional power amplifiers, effectively mitigating excessive high-frequency signal attenuation and low signal-to-noise ratios in long-distance transmission lines. Using this topology, a three-phase differential-frequency coordinated excitation test platform is developed to ensure the accurate, synchronous injection of isolated three-phase differential-frequency sinusoidal waveforms into the cable sending end. Combined with broadband impedance spectra acquired by the test system, the proposed diagnostic model enables the reliable identification of defect and fault types in three-phase cross-bonded cables, offering practical significance for the safe and stable operation of power transmission systems.

Keywords: cross-bonded cable; broadband impedance spectroscopy; differential frequency decoupling; high-frequency high-voltage excitation; defect diagnosis

Check for updates

Academic Editor: Valeri Mladenov

Received: 8 August 2026
Revised: 29 August 2026
Accepted: 31 August 2026
Published: 7 September 2026

Correction Statement: This article has been republished with a minor change. The change does not affect the scientific content of the article and further details are available within the backmatter of the website version of this article.

Copyright: © 2026 by the authors. Licensee MDPI, Basel, Switzerland. This article is an open access article distributed under the terms and conditions of the Creative Commons Attribution (CC BY) license.

1. Introduction

With the continuous advancement of urban modernization, the proportion of long-distance high-voltage cables in power transmission networks has increased rapidly. Cross-linked polyethylene cables have become the mainstream solution for underground power transmission due to their excellent electrical performance and operational reliability [1,2]. To minimize line losses, high-voltage cables are typically laid with three-phase cross-bonded grounding schemes. Over long-term service, however, these cables are prone to various defects and faults driven by overload heating, moisture ingress, and insulation aging [3].

Therefore, accurately diagnosing defect and fault types in three-phase cross-bonded cables is of paramount importance for the safe and stable operation of transmission systems [4,5].

Conventional cable defect detection techniques include partial discharge testing, reflectometry, and broadband impedance spectroscopy [6]. High-frequency partial discharge detection utilizes high-frequency current transformers to couple discharge pulses within a frequency range of 10 kHz to 100 MHz from cable grounding leads, evaluating defect severity based on pulse amplitude and repetition frequency [7]. However, this approach suffers from severe signal attenuation and a limited detection range. Discharge signals originating from the defective phase can easily couple to the sheaths of the adjacent two phases, making it virtually impossible to determine the phase sequence and exact location of the discharge source. Furthermore, on-site harmonics and ambient radio frequency signals frequently interfere with detection results.

Reflectometry methods locate defects by analyzing the arrival time difference between the injected excitation signal and the reflected wave; however, they remain strongly affected by inter-cable signal coupling and still fail to identify the defective phase sequence [8]. Time-Domain Reflectometry captures limited high-frequency information and is severely degraded by signal dispersion, rendering it challenging to detect early local insulation defects. In three-phase cross-bonded cables, transmitted signals are highly susceptible to inter-phase electromagnetic coupling at cross-bonding points, producing complex reflected signal characteristics that cannot be effectively decoupled to distinguish the defective phase, ultimately impairing localization accuracy over long distances. Similarly, in Frequency-Domain Reflectometry, incident and reflected waves are strongly frequency dependent, which increases the difficulty of defect identification and limits positioning precision.

Broadband impedance spectroscopy, featuring non-intrusive measurement, rich frequency domain information, and high sensitivity to early insulation degradation, has emerged as an important diagnostic tool and has been successfully applied to single-core cables [9–11]. Nevertheless, its application to three-phase cross-bonded cables faces significant constraints. First, the cross-bonded structure forms a closed loop via the three-phase sheaths, causing mutual coupling among the phase impedance spectra and complicating independent phase decoupling. Second, the output voltage amplitude of existing broadband impedance spectroscopy detectors is limited, resulting in poor identification accuracy for long-distance cables [12]. Moreover, high-frequency signals undergo substantial amplitude attenuation and phase distortion during long-distance transmission, which, when compounded by complex on-site electromagnetic interference, results in severely degraded signal-to-noise ratios. Consequently, both anti-interference capability and diagnostic accuracy require further improvement [13–15].

To address the challenges of inter-phase signal coupling and attenuation, this paper proposes a differential-frequency impedance spectroscopy decoupling method based on three-phase high-frequency, high-voltage coordinated excitation. First, considering the topology of the three-phase sheath current loop, the transposed coaxial cables within the cross-bonding box are modeled as high-frequency equivalent impedances; a complete transmission line model for the three-phase cross-bonded cable is then established to achieve differential-frequency decoupling of the head-end impedance spectrum for each phase [16]. Concurrently, a three-phase cascaded high-frequency, high-voltage amplifier is developed to resolve the severe attenuation in long-distance lines caused by low excitation amplitudes [17]. On this basis, a differential-frequency coordinated excitation strategy is implemented to synchronously inject differential-frequency, high-voltage sinusoidal signals into the three-phase cable, enabling the decoupled extraction of broadband impedance characteristics across the cross-bonded system. Finally, diagnostic criteria for insulation

defects and faults are formulated based on these broadband impedance features, achieving accurate cable defect and fault diagnosis [18].

2. Decoupling Model of Three-Phase Cross-Bonded Cable Transmission Lines

2.1. Establishment of the Decoupling Model for Cross-Bonded Cables

The structure of a cross-bonded cable is shown in Figure 1. A single main section consists of nine metal sheath units A_1–C_3 for the three phases and six sets of intermediate joints J_1–J_6. Direct grounding boxes GB1 and GB2 are arranged at both ends of the system, and sheath transposition is completed through two cross-bond boxes CB1 and CB2 within the section. To meet the requirements of signal transmission path consistency and anti-interference ability for broadband impedance spectroscopy detection, medium-voltage (MV) coaxial cables are commonly used as sheath connection leads [19].

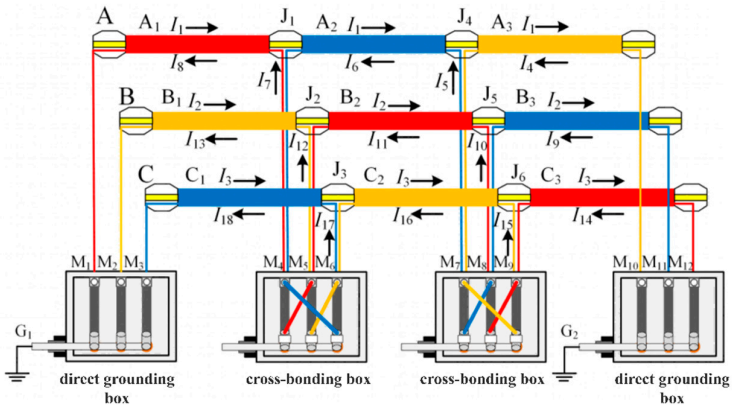


Figure 1. Electrical topology diagram of cross-bonded cable transposition.

In practical installations, each sheath unit is connected to its corresponding cross-bonding box and direct grounding box via coaxial leads inside the joint. Taking the Phase A loop as an example, at joint J_1, the sheaths of sections A_1 and A_2 are connected to the inner conductor and metallic shield of coaxial M_4, respectively. Similarly, at joint J_4, the sheaths of A_2 and A_3 are connected to the inner conductor and shielding layer of coaxial cable M_7 in the same manner.

According to the topology shown in Figure 2, an equivalent transmission line model is established using Phase A of the three-phase cross-bonded cable as the research object. The per-unit-length distributed parameters of the three-phase cross-bonded cable are defined as resistance R_1, inductance L_1, G_1, and C_1, respectively. The corresponding distributed parameters of the medium-voltage cable in the cross-bonded section are denoted as R_2, L_2, G_2, and C_2, respectively. When analyzing the electrical coupling characteristics and current transmission laws of cable Mi, let I_{15} and I_{12} represent the induced currents flowing through the metallic sheaths of M9 and M5, respectively. Because the electrical length of the medium-voltage cross-bonding connection cable is much smaller than the signal wavelength, its distributed parameter effects can be ignored, and the propagation loss along the lead can be approximately neglected. Consequently, the equivalent impedance of the medium-voltage cable can be represented by the lumped parameter Z_m, leading to the equivalent circuit model depicted in Figure 3.

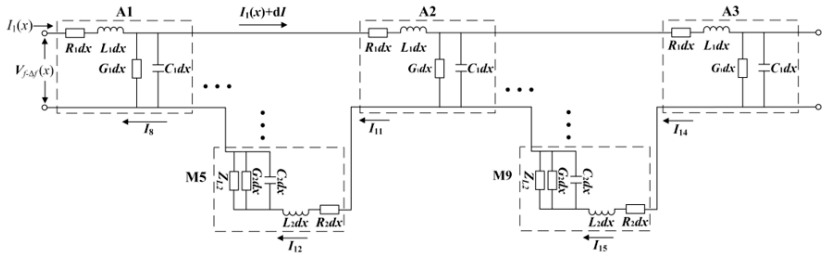


Figure 2. Transmission line model of three-phase cross-bonded cable system.

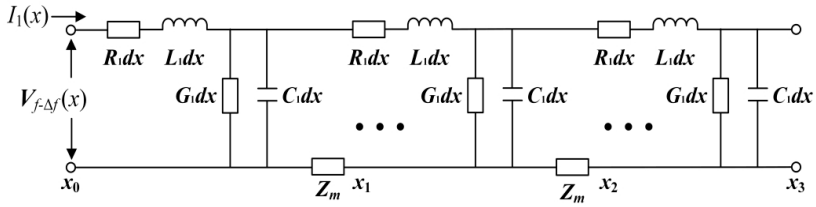


Figure 3. Simplified equivalent circuit diagram of three-phase cross-bonded cable system.

2.2. Analysis of the Transmission Line Model for Three-Phase Cross-Bonded Cables

According to classical lossy transmission-line theory [20], high-frequency signal propagation in cables can be described by a distributed-parameter transmission-line model, in which the propagation constant, characteristic impedance, voltage, and current satisfy the corresponding fundamental transmission relationships. Based on this theory, a high-frequency equivalent transmission-line model for three-phase cross-bonded cables is established by considering the sheath transposition configuration and the corresponding signal transmission paths, and the voltage and current transmission relationships for different cable sections are further derived.

Unless otherwise specified, the voltage and current quantities used in the following frequency-domain transmission-line analysis are represented by complex phasors. Instantaneous quantities are denoted by lowercase letters $v(t)$ and $i(t)$, while RMS quantities are explicitly indicated by the subscript "rms". Impedance quantities are represented as complex quantities Z, and their magnitudes are denoted by $|Z|$.

Let $V_{f-\Delta f(x)}$ represent the excitation voltage at the sending end of Phase A, and let Z_L denote the terminal impedance. Setting the sending end of the cable as the coordinate origin x_0, the total length of a single-phase cable is defined as L. In a three-phase cross-bonded system, the metallic sheath is not electrically continuous but is transposed at the cross-bonding joints located at coordinates x_1 and x_2, while the cable terminal load side corresponds to position $x_3 = L$.

In the section extending from the final sheath transposition joint to the cable terminal where $x_2 \le x \le x_3$, the signal propagation behavior is identical equivalent to that of a conventional transmission line. The voltage and current in this section are primarily formed by the superposition of the forward-propagating incident wave and the reflected wave caused by terminal impedance mismatch.

$$V(x) = V^+ e^{\gamma(L-x)}(1 + \Gamma_L e^{-2\gamma(L-x)}) \tag{1}$$

$$I(x) = \frac{V^+ e^{\gamma(L-x)}}{Z_0}(1 - \Gamma_L e^{-2\gamma(L-x)}) \tag{2}$$

In the middle section where $x_1 \le x \le x_2$, the coupling term at joint x_2 must be incorporated into the voltage expression:

$$\dot{V}(x) = V^+ e^{\gamma(L-x)}\left(1 + \Gamma_L e^{-2\gamma(L-x)}\right) - Z_m I_{x_2}\left(e^{\gamma(x_3-x)} + e^{-\gamma(x_3-x)}\right) \tag{3}$$

$$I(x) = \frac{V^{+}e^{\gamma(L-x)}}{Z_0}(1 - \Gamma_L e^{-2\gamma(L-x)}) \tag{4}$$

For $x_0 \le x \le x_1$, the high-frequency signal is affected by both cross-bonding points, resulting in the most complex voltage waveform distortion:

$$\dot{V}(x) = V^{+}e^{\gamma(L-x)}\left(1 + \Gamma_L e^{-2\gamma(L-x)}\right) - Z_m I_{x_2}\left(e^{\gamma(x_3-x)} + e^{-\gamma(x_3-x)}\right) - Z_m I_{x_1}\left(e^{\gamma(x_3-x)} + e^{-\gamma(x_3-x)}\right) \tag{5}$$

$$I(x) = \frac{V^{+}e^{\gamma(L-x)}}{Z_0}\left(1 - \Gamma_L e^{-2\gamma(L-x)}\right) \tag{6}$$

where V^{+} is the head-end excitation voltage, Γ_L is the load reflection coefficient, γ is the propagation constant, and Z_0 is the characteristic impedance:

$$\Gamma_{\mathrm{L}} = \frac{Z_{\mathrm{L}} + Z_{\mathrm{C}}}{Z_{\mathrm{L}} - Z_{\mathrm{C}}} \tag{7}$$

$$\gamma = \sqrt{(R_0 + \mathrm{j}\omega L_0)(G_0 + \mathrm{j}\omega C_0)} = \alpha + \mathrm{j}\beta \tag{8}$$

$$Z_0 = \sqrt{\frac{R_1 + \mathrm{j}\omega L_1}{G_1 + \mathrm{j}\omega C_1}} \tag{9}$$

where α and β are the attenuation constant and phase constant, respectively.

Based on the transmission-line model established above, the head-end input impedance of the healthy three-phase cross-bonded cable is further derived in this study as:

$$\begin{aligned} Z_{\mathrm{h}} = \frac{V(L)}{I(L)} = Z_0\left(\frac{1+\Gamma_L e^{-2\gamma L}}{1-\Gamma_L e^{-2\gamma L}}\right) - Z_{\mathrm{m}}\frac{(1+e^{-2\gamma x_1} - \Gamma_L e^{-2\gamma L}(1+e^{2\gamma x}))}{(1-\Gamma_L e^{-2\gamma L})} - \\ Z_{\mathrm{m}}\frac{(1+e^{-2\gamma x_2} - \Gamma_L e^{-2\gamma L}(1+e^{2\gamma x_2}))}{(1-\Gamma_L e^{-2\gamma L})} \end{aligned} \tag{10}$$

2.3. Analysis of the Transmission Line Model for Three-Phase Cross-Bonded Cables with Defects and Faults

In cable transmission lines, the gradual development of cable body insulation defects will lead to system faults in severe cases [21]. This paper first investigates the influence of insulation defects on the distribution of the head-end impedance spectrum distribution. Since the two types of commonly occurring insulation defects in high-voltage cable engineering are XLPE main insulation thermal aging and metallic shielding layer damage, they correspond to abnormal increase and abnormal decrease of the equivalent capacitance of the insulation layer in the distributed parameter model, respectively [22]. It is assumed that an insulation defect section with a length of Δl_d exists in section A3 of the three-phase cross-bonded cable, and its equivalent transmission model is shown in Figure 4.

Based on the transmission-line model established above, this study further establishes an equivalent transmission-line model for a three-phase cross-bonded cable containing a local insulation defect. Let Z_{L} denote the terminal impedance, x_{d} denote the starting position of the defect section, and Δl_{d} denote the defect length. According to the impedance transformation and reflection relationships on both sides of the defect section, the reflection coefficient Γ_1 and the input impedance at $x = x_{\mathrm{d}} + \Delta l_{\mathrm{d}}$ are derived as

$$\Gamma_1 = \frac{Z_{\mathrm{L}} - Z_{0_{\mathrm{h}}}}{Z_{\mathrm{L}} + Z_{0_{\mathrm{h}}}} \tag{11}$$

$$Z_{(x_{\mathrm{d}}+\Delta l_{\mathrm{d}})} = Z_{0\mathrm{h}}\frac{1 + \Gamma_1 \mathrm{e}^{-2\gamma_{\mathrm{h}}(L - x_{\mathrm{d}} - \Delta l_{\mathrm{d}})}}{1 - \Gamma_1 \mathrm{e}^{-2\gamma_{\mathrm{h}}(L - x_{\mathrm{d}} - \Delta l_{\mathrm{d}})}} \tag{12}$$

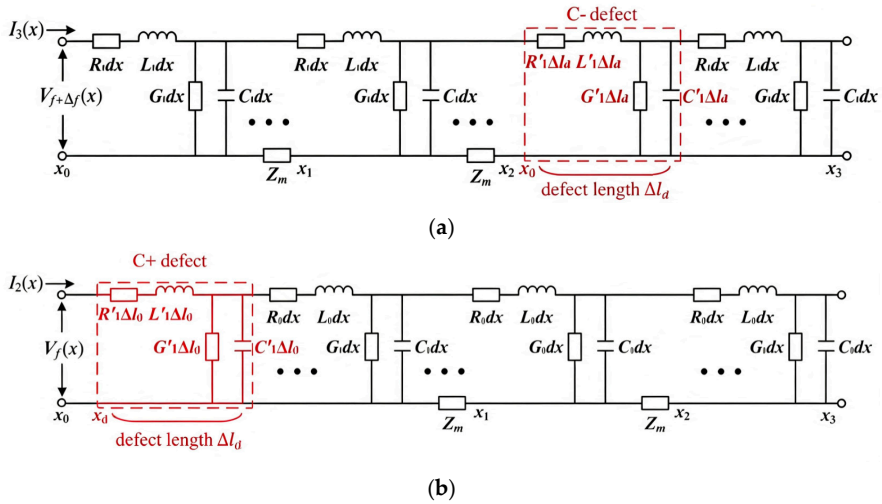


Figure 4. Transmission line model of cable with insulation defects. (**a**) Equivalent model with C− defect. (**b**) Equivalent model with C+ defect.

To simplify the boundary condition, the cable terminal is assumed to be open-circuited, i.e., $\Gamma_1 = 1$. By substituting this boundary condition into the above expressions and applying the impedance transformation relationships within and on both sides of the defect section, the reflection coefficient Γ_2 and the input impedance $Z(x_\mathrm{d})$ are further derived as

$$\Gamma_2 = \frac{Z_{0\mathrm{h}}(1+e^{-2\gamma_\mathrm{h}(L-x_\mathrm{d}-\Delta l_\mathrm{d})}) - Z_{0\mathrm{d}}(1-e^{-2\gamma_\mathrm{h}(L-x_\mathrm{d}-\Delta l_\mathrm{d})})}{Z_{0\mathrm{h}}(1+e^{-2\gamma_\mathrm{h}(L-x_\mathrm{d}-\Delta l_\mathrm{d})}) + Z_{0\mathrm{d}}(1-e^{-2\gamma_\mathrm{h}(L-x_\mathrm{d}-\Delta l_\mathrm{d})})} = \frac{\mathrm{A}-\mathrm{B}}{\mathrm{A}+\mathrm{B}} \tag{13}$$

$$\begin{aligned} Z(x_\mathrm{d}) &= Z_{0\mathrm{d}}\frac{1+\Gamma_2 e^{-2\gamma_\mathrm{h}x_d}}{1-\Gamma_2 e^{-2\gamma_\mathrm{h}x_d}} = Z_{0\mathrm{d}}\frac{A\left(1+e^{-2\gamma_\mathrm{d}\Delta l_\mathrm{d}}\right)+B\left(1-e^{-2\gamma_\mathrm{d}\Delta l_\mathrm{d}}\right)}{A\left(1-e^{-2\gamma_\mathrm{d}\Delta l_\mathrm{d}}\right)+B\left(1+e^{-2\gamma_\mathrm{d}\Delta l_\mathrm{d}}\right)} \\ &= Z_{0\mathrm{d}}\frac{AC+BD}{AD-BD} \end{aligned} \tag{14}$$

where A represents the equivalent transmission characteristics of the healthy cable section downstream of the defect section; B represents the impedance combination relationship resulting from the joint effects of the characteristic impedance of the defect section and the propagation characteristics of the downstream healthy cable section; and C and D are propagation characteristic combination terms of the defect section, which characterize the effects of the propagation constant γ_d and defect length Δl_d on the round-trip propagation of high-frequency signals.

By treating the defect section as an equivalent load and transforming its impedance toward the cable head end, the reflection coefficient Γ_3 at the starting position of the defect section is further derived from the impedance discontinuity on both sides of the defect point as:

$$\Gamma_3 = \frac{Z_{0\mathrm{d}}(AC+BD) - Z_{0\mathrm{h}}(AD+BC)}{Z_{0\mathrm{d}}(AC+BD) + Z_{0\mathrm{h}}(AD+BC)} = \frac{Z(x_\mathrm{d}) - Z_{0\mathrm{h}}}{Z(x_\mathrm{d}) + Z_{0\mathrm{h}}} = \frac{E-F}{E+F} \tag{15}$$

$$Z(x_2) = Z_{0h}\frac{E\left(1+\Gamma_3 e^{-2\gamma_\mathrm{h}x_d}\right)+F\left(1-\Gamma_3 e^{-2\gamma_\mathrm{h}x_d}\right)}{E\left(1-\Gamma_3 e^{-2\gamma_\mathrm{h}x_d}\right)+F\left(1+\Gamma_3 e^{-2\gamma_\mathrm{h}x_d}\right)} = Z_{0h}\frac{1+\Gamma_3 e^{-2\gamma_\mathrm{h}x_d}}{1-\Gamma_3 e^{-2\gamma_\mathrm{h}x_d}} \tag{16}$$

The transmission impedances of Sections A1 and A2 are then equivalently transformed to the terminal position x_2, and the resulting equivalent impedance is denoted by $\mathrm{Z_{eq}}$. Accordingly, the head-end input impedance Z_in is further derived as:

$$\mathrm{Z_{in}} = \frac{\mathrm{Z_{0h}}\cdot\mathrm{Z_{eq}}\left[\mathrm{E}\left(1+\mathrm{e}^{-2\gamma_\mathrm{h}x_\mathrm{d}}\right)+\mathrm{F}\left(1-\mathrm{e}^{-2\gamma_\mathrm{h}x_\mathrm{d}}\right)\right]}{\mathrm{Z_{0h}}\left[\mathrm{E}\left(1+\mathrm{e}^{-2\gamma_\mathrm{h}x_\mathrm{d}}\right)+\mathrm{F}\left(1-\mathrm{e}^{-2\gamma_\mathrm{h}x_\mathrm{d}}\right)\right]+\mathrm{Z_{eq}}\left[\left(1-\mathrm{e}^{-2\gamma_\mathrm{h}x_\mathrm{d}}\right)+\mathrm{F}\left(1+\mathrm{e}^{-2\gamma_\mathrm{h}x_\mathrm{d}}\right)\right]} \tag{17}$$

It can be seen from Equation (17) that the input impedance at the test terminal can effectively map the characteristic parameters of locally damaged sections such as γ_d and Δl_d, thereby causing resonance point offset and amplitude change of the cable impedance spectrum.

Next, the cable impedance spectrum in the case of cable fault is analyzed. Taking a fault in section C_3 as an example, its equivalent distributed parameter model is shown in Figure 5.

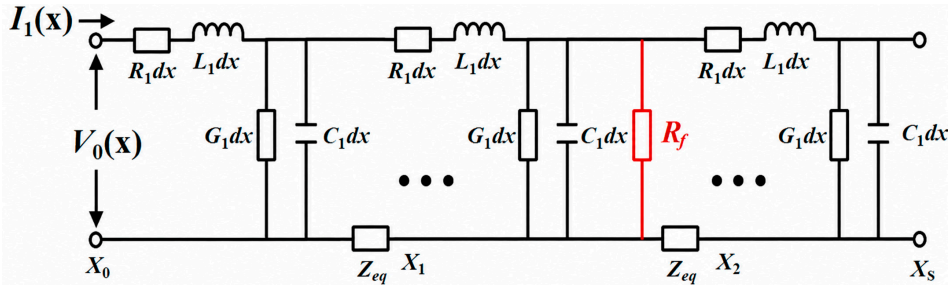


Figure 5. Equivalent model of faulty three-phase cross-bonded cable.

R_f denotes the local equivalent fault impedance at the fault point. When simulating cable fault conditions, the electrical parameters at the fault node are usually simplified to a lumped equivalent impedance R_f. The magnitude of this impedance is generally set as $R_f = kZ_0$, where the coefficient k is used to characterize the specific type of insulation fault. When $k = 0$, the cable is considered to have a short-circuit fault; when $0 < k < 10$, it is considered a low-resistance fault; when $10 < k < \infty$, it is considered a high-resistance fault; when $k = \infty$, it is considered an open-circuit fault.

The input impedance at the cable head end $x_0 = 0$ and the input impedance at $x = x_f$ are, respectively,

$$\mathrm{Z}(0) = \mathrm{Z_h}\left(\frac{1+\Gamma_{\mathrm{L1}}\mathrm{e}^{-2\gamma_\mathrm{h}\mathrm{x_f}}}{1-\Gamma_{\mathrm{L1}}\mathrm{e}^{-2\gamma_\mathrm{h}\mathrm{x_f}}}\right) \tag{18}$$

$$Z(x_f) = Z_h\left(\frac{1+\Gamma_L e^{-2\gamma_h x_f}}{1-\Gamma_L e^{-2\gamma_h x_f}}\right) \tag{19}$$

Accordingly, the reflection coefficient at the fault point is derived as

$$\begin{aligned} Z(x_2) &= Z_{0h}\frac{E\left(1+\Gamma_3 e^{-2\gamma_\mathrm{h}x_d}\right)+F\left(1-\Gamma_3 e^{-2\gamma_\mathrm{h}x_d}\right)}{E\left(1-\Gamma_3 e^{-2\gamma_\mathrm{h}x_d}\right)+F\left(1+\Gamma_3 e^{-2\gamma_\mathrm{h}x_d}\right)} \\ &= Z_{0h}\frac{1+\Gamma_3 e^{-2\gamma_\mathrm{h}x_d}}{1-\Gamma_3 e^{-2\gamma_\mathrm{h}x_d}} \end{aligned} \tag{20}$$

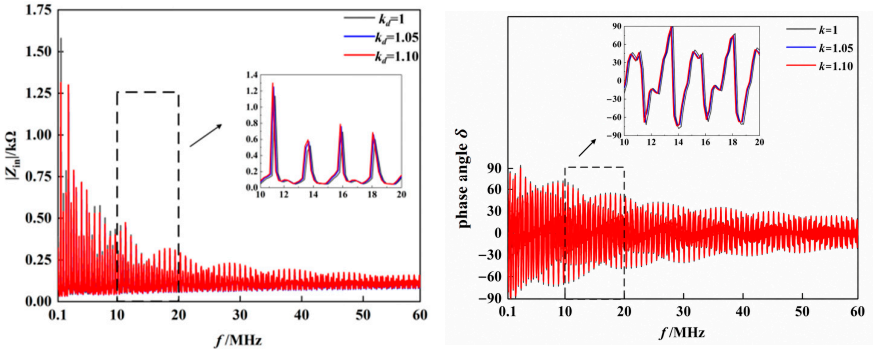
In this paper, the cable terminal is set to an open-circuit state, and the cable terminal reflection coefficient Γ_L is 1 at this time.

3. Simulation Analysis of Impedance Spectra for Cables with Defects and Faults

3.1. Simulation Analysis of Impedance Spectra for Cables with Defects

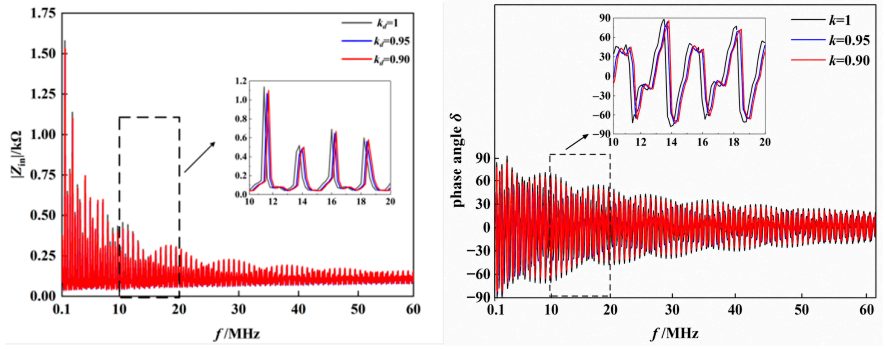
To quantitatively analyze the above theoretical derivation, this paper carries out a simulation calculation based on MATLAB (R2024b). The simulation object selects a YJLV 8.7/15 kV XLPE cable with a total length of 1500 m, and all three phases are cross-bonded and transposed at nodes x = 500 m and x = 1000 m. The frequency sweep range is set from 100 kHz to 60 MHz, with a frequency sampling step of 500 Hz. A defect severity coefficient k_d is introduced to characterize the severity of insulation damage, i.e., the equivalent capacitance of the defect section $C'_1 = k_d C_1$. Taking Phase A as a healthy reference cable,

C+ defect sections with a length of 10 cm are configured at x = 300 m in Phase B using k_d = 1.05 and k_d = 1.10, while C− defect sections with a length of 5 cm are configured at x = 1200 m in Phase C using k_d = 0.95 and k_d = 0.90. The obtained impedance spectra are shown in Figures 6 and 7.



(**a**) Amplitude spectrum of C+ defect (**b**) Phase spectrum of C+ defect

Figure 6. Input impedance spectra under C+ defects.



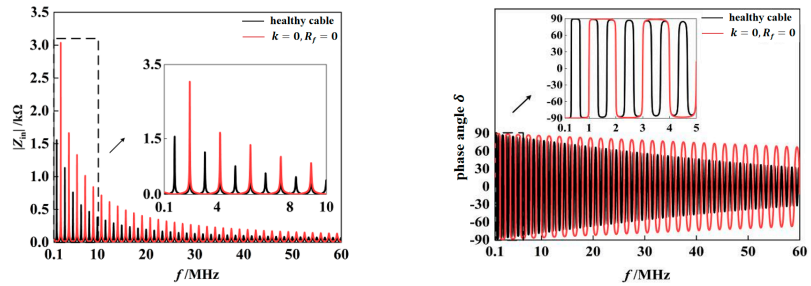
(**a**) Amplitude spectrum of C− defect (**b**) Phase spectrum of C− defect

Figure 7. Input impedance spectra under C− defects.

As demonstrated by the simulation results in Figures 6 and 7, both C+ and C− defects induce resonant peak amplitude variations in the amplitude spectrum and a global phase shift in the phase spectrum. For C+ defects, the phase spectrum shifts to the left as a whole. Conversely, for C− defects, the phase spectrum shifts to the right as a whole, with the shift magnitude positively correlated with both the defect length Δl_d and the defect severity k_d. Importantly, the initial phase values for both categories of body insulation defects remain at −90°.

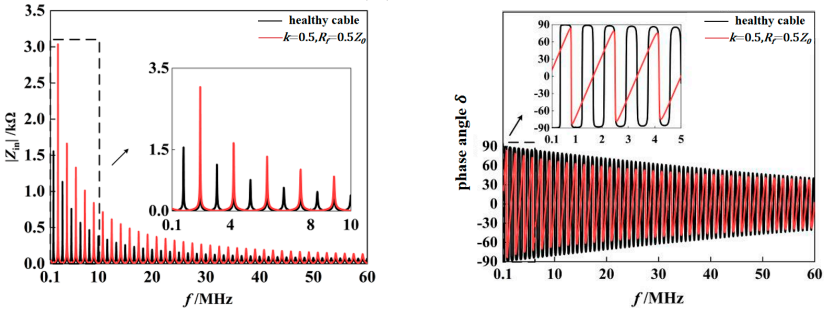
3.2. Simulation Analysis of Impedance Spectra for Cables with Faults

To investigate how the fault severity coefficient k influences the sending-end input impedance during system faults, simulations were conducted on the same YJLV 8.7/15 kV cable model with a total length of L = 1500 m and a frequency sweep range from 0.1 MHz to 60 MHz. The fault position was set at x_f = 750 m from the sending end, and the characteristic impedance Z_0 of the test cable calculated by Equation (9) to be 32.56 Ω. Four typical fault categories were simulated based on the equivalent fault resistance R_f: a short-circuit fault where $R_f = 0$, a low-resistance fault where $R_f = 5Z_0$, high-resistance faults where $R_f = 11Z_0$ and $R_f = 50Z_0$, and an open-circuit fault where $R_f = \infty$ (Figure 8).



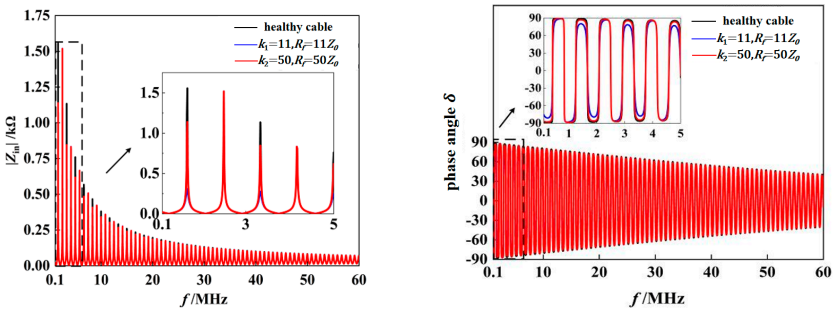
(**a**) Amplitude spectrum of short-circuit fault (**b**) Phase spectrum of short-circuit fault

(**A**) $R_f = 0$



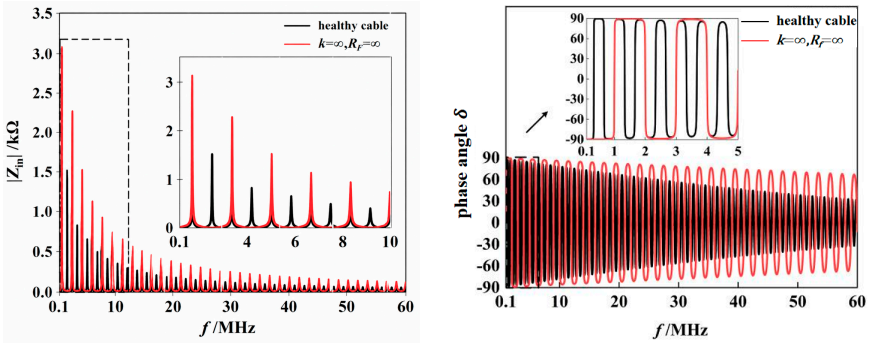
(**a**) Amplitude spectrum of low-resistance fault (**b**) Phase spectrum of low-resistance fault

(**B**) $R_f = 5Z_0$



(**a**) Amplitude spectrum of high resistance fault(**b**) Phase spectrum of high resistance fault

(**C**) $R_f = 11Z_0, R_f = 50Z_0$



(**a**) Amplitude spectrum of open-circuit fault (**b**) Phase spectrum of open-circuit fault

(**D**) $R_f = \infty$

Figure 8. Impedance spectra of faulty cables.

According to Equations (18)–(20), the equivalent fault impedance R_f changes the input impedance and reflection coefficient at the fault point, thereby affecting the reflected-wave component and the head-end input impedance Z_{in}. Consequently, different values of $R_f = kZ_0$ lead to different resonance amplitudes, resonance periods, and initial phase characteristics. A short-circuit fault ($R_f = 0$) produces strong reflection with phase reversal, resulting in increased resonant peaks, an increased resonant period, and a change in the initial phase from $-90°$ to $+90°$. For a low-resistance fault, the finite fault impedance changes the

impedance discontinuity at the fault point, causing reduced resonant peaks, an increased resonant period, and an initial phase between 0°and +90°. For a high-resistance fault, the influence of the fault branch weakens as R_f increases; therefore, the resonant frequencies remain nearly unchanged, while the peak attenuation gradually decreases and the initial phase remains between −90°and 0°. As R_f approaches infinity, the fault point approaches an open-circuit boundary, resulting in increased resonant peaks and an increased resonant period, while the initial phase remains at −90○. These variations are consistent with the dependence of the fault-point reflection coefficient and Z_{in} on R_f described by Equations (18)–(20).

Based on the aforementioned impedance spectrum simulation results and the extracted key characteristic quantities, this paper proposes a multi-dimensional parameter collaborative diagnosis model as shown in Figure 9.

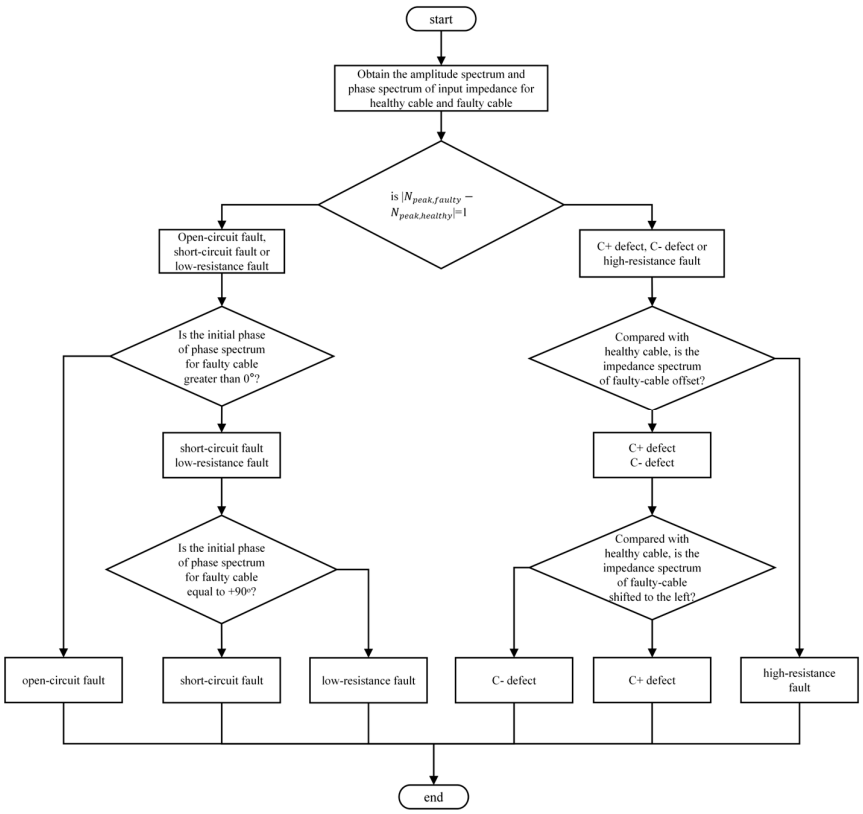


Figure 9. Multidimensional parameter-based collaborative diagnosis model.

4. Principle of Three-Phase High-Voltage High-Frequency Coordinated Excitation

Design of High-Frequency High-Voltage Linear Cascade Amplification Topology

Conventional power amplifiers and spectrum analyzers generally have limited output capabilities. For instance, the full-power bandwidth of the Trek 2100HF power amplifier is limited to 2.6 MHz, whereas the maximum AC output voltage of a WK6500B spectrum analyzer reaches only approximately 1 V. Consequently, these instruments cannot satisfy the driving requirements of three-phase high-frequency high-voltage coordinated excitation systems. Particularly during the testing of three-phase cross-bonded cables, weak AC detection signals undergo significant attenuation, which ultimately distorts the spectral characteristics [23]. To overcome this technical bottleneck, a novel high-frequency high-voltage cascaded amplification topology based on parallel optical-fiber isolation technology was developed. This topology achieves an effective operating bandwidth of 100 MHz.

When sixteen single-stage circuit units are cascaded, the system stably outputs a linear high-voltage signal of 192 Vpp.

As illustrated in the circuit configuration in Figure 10, the core architecture employs cascaded single-stage isolated-drive differential topologies to achieve progressive voltage amplification. Theoretically, connecting n single-stage units in series expands the overall loop gain by a factor of 6n, allowing the differential output voltage amplitude to reach at least 12n Vpp. In this circuit topology, bias voltages BIAS1 through BIASn correspond to the reverse-bias voltages of each stage of the avalanche photodetectors. At the excitation source end, an arbitrary waveform generator (VS0) produces reference signals spanning the kilohertz to megahertz frequency band according to control instructions from the host computer software. These reference signals modulate and drive a distributed feedback laser to emit high-power optical beams. To ensure that the output signals across all cascaded amplification units remain consistent in both amplitude and initial phase, the laser energy distribution and spatial directivity received by each avalanche photodetector stage must remain consistent. Under these conditions, an equal-ratio optical splitting technique is implemented to perform synchronous high-speed optical fiber driving. This scheme eliminates the electrical connection between the input signal source and the power amplification stage, thereby achieving complete electrical isolation.

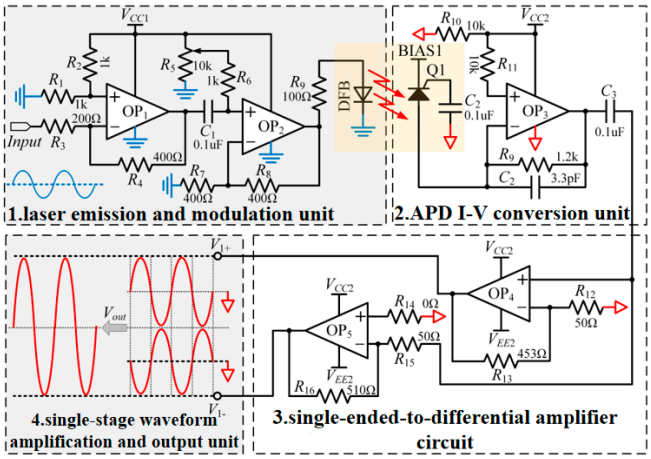


Figure 10. Single-stage isolated-drive differential amplification topology.

As shown in Figure 11, a three-phase coordinated excitation experimental system was constructed. In the excitation output stage, the host computer transmits control commands to schedule the high-frequency signal generator, producing three channels of digital waveforms with distinct frequencies, specifically $f - \Delta f$, f and $f + \Delta f$, in parallel. These three reference signals are amplified by the high-voltage cascaded amplification modules corresponding to Phase A, Phase B, and Phase C, respectively. Consequently, high-voltage sinusoidal waveforms possessing differential frequency characteristics are synchronously injected into the sending end of the tested cable. In the response measurement stage, weak current signals from each phase loop are converted into voltage parameters via current-to-voltage conversion circuits. Multichannel synchronous sampling is subsequently performed using a virtual digital storage oscilloscope, and the acquired data are transmitted back to the host computer system in real time for subsequent impedance spectrum analysis.

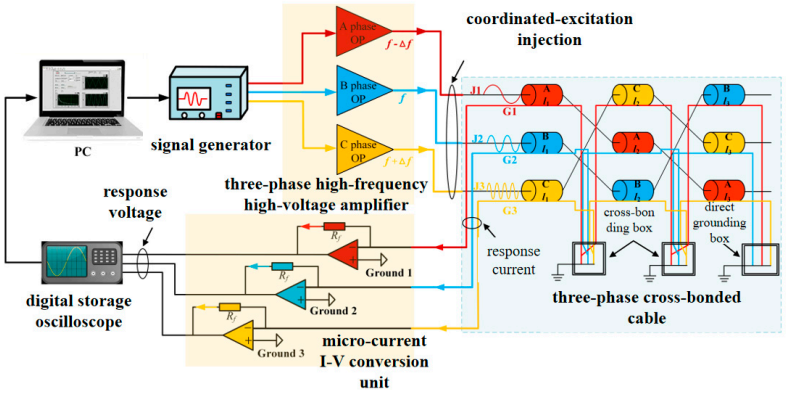


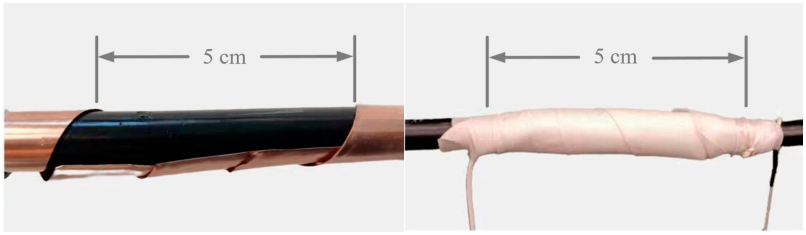
Figure 11. Principle diagram of the three-phase coordinated excitation experimental system.

5. Experimental Design and Analysis

5.1. Experimental Scheme Design

Two three-phase cross-linked polyethylene cable test loops were constructed in a laboratory environment to validate the effectiveness of the proposed diagnostic method. In these experiments, six sections of YJLV 8.7/15 kV cross-linked polyethylene cables, each with a length of 120 m, were divided into two experimental groups. Three sections in each group formed a complete three-phase cross-bonded grounding system. To accurately replicate the actual operating environment of power cables, cross-bonding transposition boxes were installed at locations 40 m and 80 m from the sending end in an identical manner for both groups. To perform comparative analyses of impedance characteristics under various insulation conditions, specific defect and fault conditions were introduced into the three-phase cables of the two groups.

In the first group of cross-bonded cables, phase A serves as the reference control benchmark with an intact cable structure. For Phase B, a shielding layer structural defect representing a C- was created at position x_4 = 20 m, as shown in Figure 12a, with a defect length Δl_d of 5 cm. For Phase C, a localized thermal aging defect representing a C+ condition was introduced at position x_5 = 100 m, as shown in Figure 12b, with a defect length Δl_d of 10 cm.



(**a**) (**b**)

Figure 12. Insulation defect section of the main body. (**a**) Missing shielding layer (**b**) Part of cable with local thermal aging.

The second group of three-phase cross-bonded cables:

In the second group of three-phase cross-bonded cables, Phase A again remains intact as the defect-free benchmark reference. For Phase B, open-circuit and short-circuit faults were sequentially configured at a distance of 60 m from the sending end. The open-circuit fault was implemented by severing the conductor, whereas the short-circuit fault was created by directly shorting two leads. For Phase C, a low-resistance fault with a series impedance of 150 Ω as well as high-resistance faults with series impedances of 1 kΩ and 10 kΩ were sequentially established at a distance of 60 m from the sending end (Figure 13).

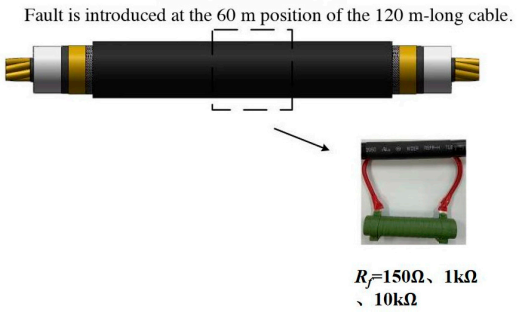


Figure 13. Simulation of different system faults.

To satisfy the synchronous detection requirements for three-phase cables, an automated testing platform depicted in Figure 14 was employed to obtain impedance characteristics. The system digitally defines the three-phase differential frequency excitation via the host PC and outputs isolated high-frequency high-voltage signals with a peak-to-peak amplitude of 128 Vpp using an eight-stage amplifier array, thereby achieving physical-layer decoupling of excitation sources. Within the measurement loop, weak current responses are converted by current-to-voltage conversion units, and multi-channel synchronous signal sampling is completed using the digital storage oscilloscope. The frequency sweep range spans from 100 kHz to 60 MHz with a frequency step of 500 Hz, enabling the reconstruction of high-resolution three-phase digital impedance spectra through a synchronous analysis algorithm executed on the host PC to provide comprehensive data support for insulation defect diagnosis.

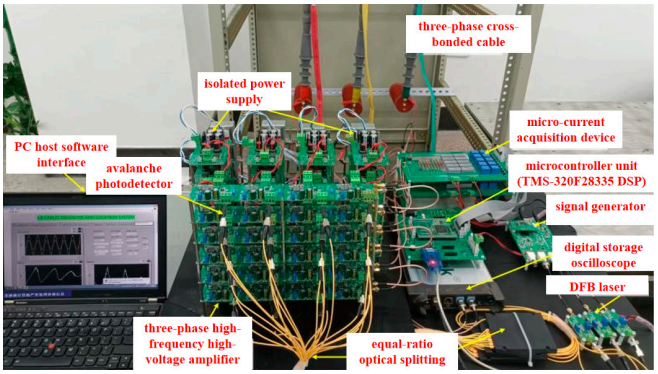
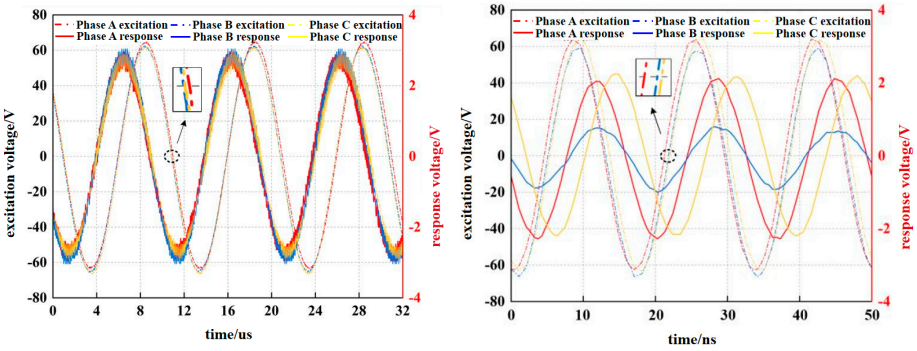


Figure 14. Three-phase high-voltage high-frequency collaborative testing system.

5.2. Experimental Results and Analysis of Impedance Spectra for Three-Phase Cross-Bonded Cables with Defects and Faults

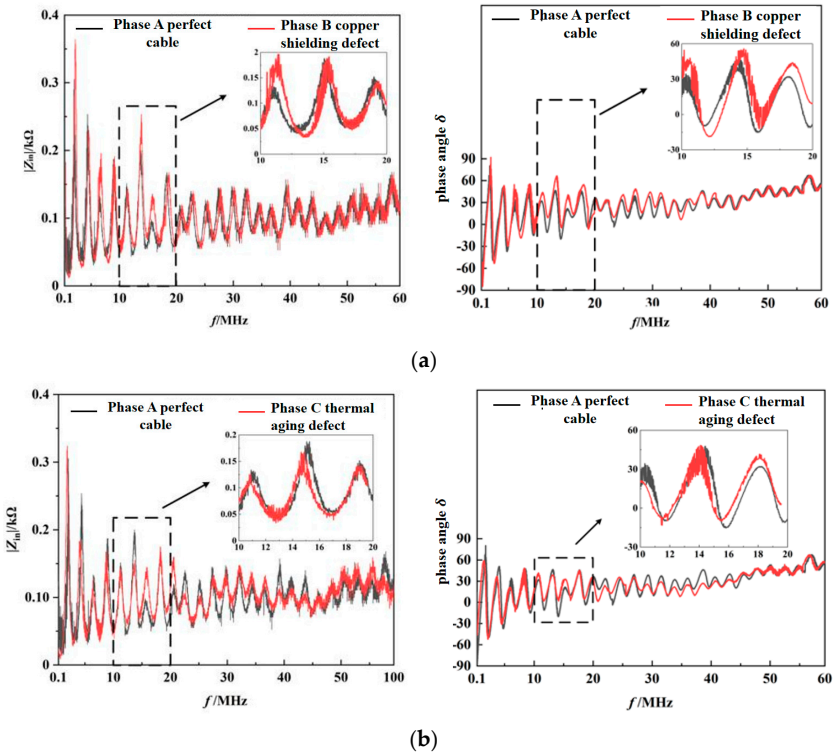
During impedance spectrum testing of three-phase cross-bonded cables containing defects and faults, isolated three-phase differential frequency excitation was applied, yielding the output waveforms shown in Figure 15. As the testing frequency increases, both the amplitude and phase angle of the output voltage exhibit pronounced periodic oscillation characteristics. When the excitation frequency approaches a system resonant point, the response current in the loop reaches its maximum amplitude, while the phase angle difference between the response current and excitation voltage reaches a minimum. Conversely, when the testing frequency deviates from the resonant center, the current attenuates accordingly, accompanied by a synchronous widening of the phase angle difference.



(**a**) 100 kHz (**b**) 60 MHz

Figure 15. Analysis of three-phase differential frequency coordinated excitation testing.

The decoupled impedance spectra obtained using the proposed test system are presented in Figure 16. Experimental results for localized cable insulation defects demonstrate that the resonant characteristics of the input impedance spectrum shift predictably according to the defect category. For C− defects characterized by decreased equivalent capacitance, the resonant frequencies shift systematically to the right. Conversely, for C+ defects characterized by increased equivalent capacitance, the resonant frequencies shift to the left as a whole. Furthermore, the magnitude of the resonant frequency shift is positively correlated with the severity of the insulation defect.



(**a**)

(**b**)

Figure 16. Experimental results of input impedance spectrum for cables with insulation defects. (**a**) Copper shielding defect (**b**) Thermal aging defects.

When different types of system faults occur in the cable, the reconstructed input impedance spectrum shown in Figure 17 displays evolution patterns distinct from those caused by simple insulation degradation. As fault severity increases, the initial phase of the impedance spectrum flips by 180°, the spectral amplitude exhibits a trend of initial decrease followed by an increase, and the overall resonant period undergoes significant attenuation.

These experimental observations align with the theoretical derivations, thereby confirming the validity of condition identification based on reconstructed impedance spectrum.

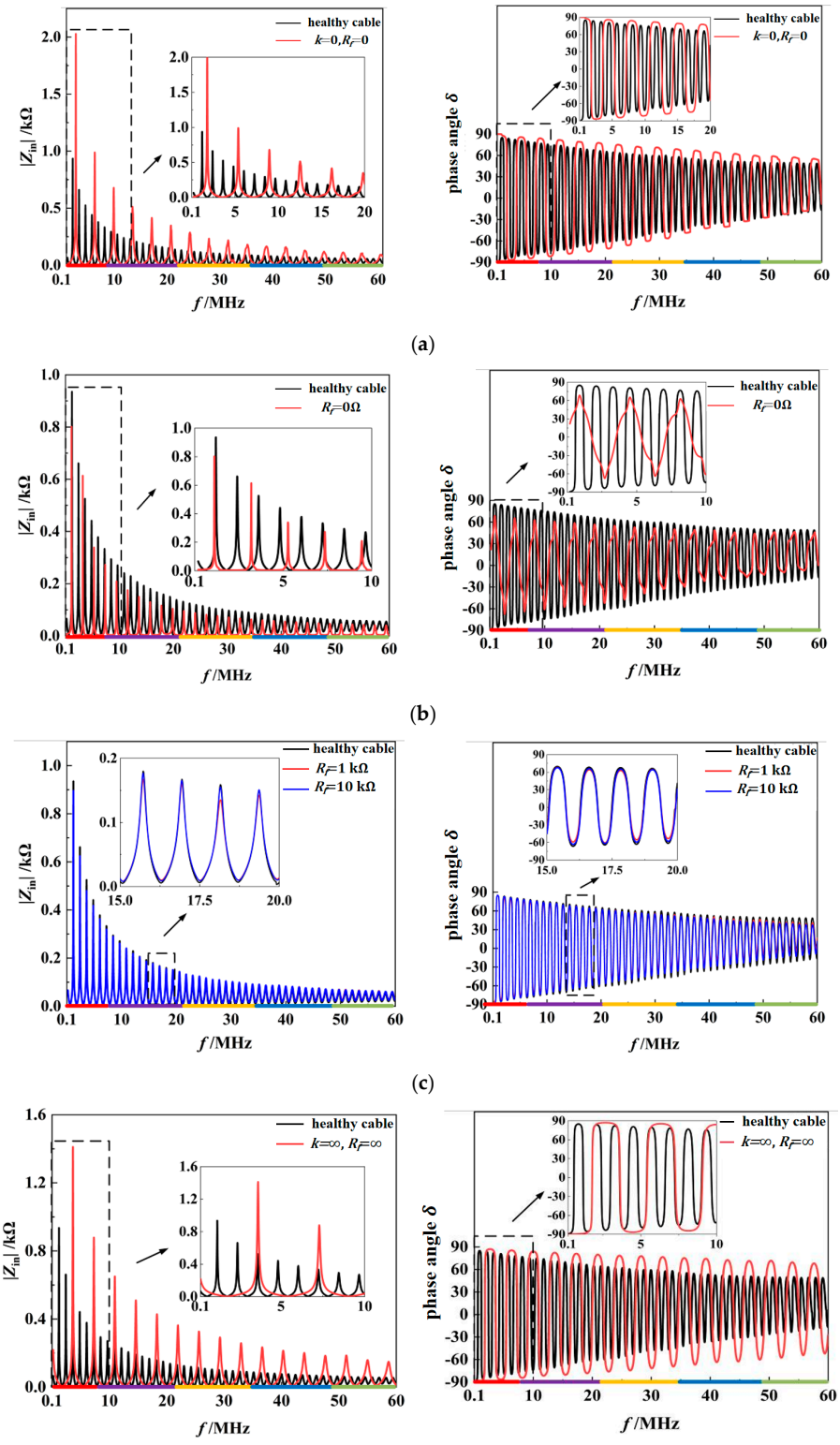


Figure 17. Impedance spectrum testing with faulty cable. (**a**) Short-circuit fault impedance spectrum (**b**) Impedance spectrum of low-resistance fault (**c**) Impedance spectrum of high-resistance fault (**d**) Open-circuit fault impedance spectrum.

To quantify frequency domain features further and achieve precise pattern recognition for defects and faults, three key characteristic parameters are extracted, namely the fundamental resonant peak amplitude variation ratio k_f, the resonant period change rate k_T, and the initial phase offset k_Ψ. Based on this set of characteristic parameters, the specific damage condition of the cable can be clearly differentiated. A multi-dimensional identification criterion is established to enable comprehensive and accurate identification of various insulation defects and faults in three-phase cross-bonded cables, as outlined in Table 1.

Table 1. Multidimensional recognition criterion.

Characteristic Parameter / Fault Type	k_f	k_T	k_ψ
C+ defect			−90°
C− defect			−90°
open-circuit fault	>1	>1	−90°
short-circuit fault	>1	>1	+90°
low-resistance fault	>1	>1	0~+90°
high-resistance fault	<1	−1	−90~0°

6. Conclusions

This paper proposes a broadband impedance spectrum decoupling and defect diagnosis method for three-phase cross-bonded cables based on three-phase high-frequency high-voltage coordinated excitation. The main conclusions are as follows:

- Based on the lossy transmission line theory, high-frequency transmission equivalent models are established for local insulation defects and system faults of cables, respectively. Through theoretical and simulation verification, the effects of parameters such as defect type and fault degree on the broadband impedance characteristics of the head end are systematically revealed. To achieve accurate identification of defect and fault types, a multi-dimensional parameter collaborative diagnosis model is constructed. The model extracts the fundamental resonant peak amplitude variation ratio, resonance period change rate, and initial phase offset, and enables accurate identification of cable body defects and system faults through multi-dimensional identification criteria.
- A three-phase high-frequency high-voltage cascaded amplification platform is designed, whose core relies on a differential cascaded amplification architecture. This hardware scheme effectively overcomes the gain-bandwidth bottleneck of traditional power amplifiers and successfully outputs high-level excitation signals in a wide frequency band. Actual measurements show that when eight series units are selected, the system can stably output a test voltage with a peak-to-peak value of 128 Vpp in the 100 MHz frequency band. In addition, the voltage level can be continuously improved by increasing the number of cascaded modules, thereby providing anti-interference guarantee for on-site measurement of long-distance cross-bonded cables.
- An experimental platform for three-phase cross-bonded cables with defects and faults is built. The three-phase high-voltage high-frequency collaborative test system is used to obtain the differential-frequency decoupled impedance spectra of three-phase cross-bonded cables with insulation defects and faults. Based on the constructed multi-dimensional parameter collaborative diagnosis model, the identification of cable defect and fault types is realized.

Author Contributions: Conceptualization, Z.L.; methodology, Z.L., X.W. and Z.Z.; software, Z.L. and Z.Z.; validation, Z.L. and X.W.; formal analysis, X.W.; investigation, Z.L., X.W. and Z.Z.; resources,

L.H.; data curation, X.W.; writing—original draft preparation, Z.L.; writing—review and editing, L.H.; visualization, Z.L.; supervision, L.H.; project administration, Z.L.; funding acquisition, L.H. All authors have read and agreed to the published version of the manuscript.

Funding: This research was funded by Research on Insulation Failure Mechanism and Fault Diagnosis and Location Key Technologies of 66 kV Cables in Cold Regions, grant number "52243725000K". This research was funded by State Grid Heilongjiang Electric Power Co., Ltd.

Data Availability Statement: The data presented in this study are available on request from the corresponding author.

Conflicts of Interest: Authors Zhongyuan Li, Xueting Wang, and Zhen Zhang were employed by State Grid Heilongjiang Electric Power Co., Ltd., Harbin, China. The remaining author declares that the research was conducted in the absence of any commercial or financial relationships that could be construed as a potential conflict of interest. The funder had no role in the study design; in the collection, analysis, or interpretation of data; in the writing of this article; or in the decision to submit it for publication.

References

1. Emdadi, K.; Gandomkar, M.; Aranizadeh, A.; Vahidi, B.; Mirmozaffari, M. Overview of Monitoring, Diagnostics, Aging Analysis, and Maintenance Strategies in High-Voltage AC/DC XLPE Cable Systems. *Sensors* **2025**, *25*, 7096. [CrossRef] [PubMed]
2. Mazzanti, G. Updated Review of the Life and Reliability Models for HVDC Cables. *IEEE Trans. Dielectr. Electr. Insul.* **2023**, *30*, 1371–1390. [CrossRef]
3. Werelius, P.; Tharning, P.; Eriksson, R.; Holmgren, B.; Gafvert, U. Dielectric spectroscopy for diagnosis of water tree deterioration in XLPE cables. *IEEE Trans. Dielectr. Electr. Insul.* **2001**, *8*, 27–42. [CrossRef]
4. Dong, X.; Yang, Y.; Zhou, C.; Hepburn, D.M. Online Monitoring and Diagnosis of HV Cable Faults by Sheath System Currents. *IEEE Trans. Power Deliv.* **2017**, *32*, 2281–2290. [CrossRef]
5. Adel Shokry, M.; Khamlichi, A.; Garnacho, F.; Malo, J.M.; Álvarez, F. Detection and Localization of Defects in Cable Sheath of Cross-Bonding Configuration by Sheath Currents. *IEEE Trans. Power Deliv.* **2019**, *34*, 1401–1411. [CrossRef]
6. Bindi, M.; Piccirilli, M.C.; Luchetta, A.; Grasso, F. A Comprehensive Review of Fault Diagnosis and Prognosis Techniques in High Voltage and Medium Voltage Electrical Power Lines. *Energies* **2023**, *16*, 7317. [CrossRef]
7. Shafiq, M.; Kutt, L.; Lehtonen, M.; Nieminen, T.; Hashmi, M. Parameters Identification and Modeling of High-Frequency Current Transducer for Partial Discharge Measurements. *IEEE Sens. J.* **2012**, *13*, 1081–1091. [CrossRef]
8. Sheng, B.; Zhou, W.; Yu, J.; Meng, S.; Zhou, C.; Hepburn, D.M. On-line PD Detection and Localization in Cross-bonded HV Cable Systems. *IEEE Trans. Dielectr. Electr. Insul.* **2014**, *21*, 2217–2224. [CrossRef]
9. Doo, S.-H.; Kwak, K.-S.; Park, J.-B. Estimation of fault location on a power line using the time-frequency domain reflectometry. *Trans. Korean Inst. Electr. Eng.* **2008**, *57*, 268–275.
10. Mu, H.-B.; Zhang, H.-T.; Zou, X.-Y.; Zhang, D.-N.; Lu, X.; Zhang, G.-J. Sensitivity Improvement in Cable Faults Location by Using Broadband Impedance Spectroscopy With Dolph-Chebyshev Window. *IEEE Trans. Power Deliv.* **2021**, *37*, 3846–3854. [CrossRef]
11. Zhixiang, D.; Shuai, W.; Haibao, M.; Zhang, D.; Zhang, G.; Pan, J.; Xu, Z. Research on nondestructive identification and location algorithm of cables with discontinuous conductor diameters based on broadband impedance spectrum. *Energy Rep.* **2023**, *9*, 965–972. [CrossRef]
12. Han, T.; Yao, Y.; Li, Q.; Huang, Y.; Zheng, Z.; Gao, Y. Locating Method for Electrical Tree Degradation in XLPE Cable Insulation Based on Broadband Impedance Spectrum. *Polymers* **2022**, *14*, 3785. [CrossRef] [PubMed]
13. Oussalah, N.; Zebboudj, Y.; Boggs, S.A. Partial discharge pulse propagation in shielded power cable and implications for detection sensitivity. *IEEE Electr. Insul. Mag.* **2007**, *23*, 5–10. [CrossRef]
14. Papazyan, R.; Pettersson, P.; Edin, H.; Eriksson, R.; Gafvert, U. Extraction of high frequency power cable characteristics from S-parameter measurements. *IEEE Trans. Dielectr. Electr. Insul.* **2004**, *11*, 261–270. [CrossRef]
15. Duan, W.; Sun, H.; Sheng, Y.; Wang, C.; Zhao, X.; Pu, L. Broadband Impedance Spectroscopy Analysis Model for Cross-Bonded Cable Systems. In Proceedings of the 2023 IEEE 4th International Conference on Electrical Materials and Power Equipment, ICEMPE 2023, Shanghai, China, 7–10 May 2023; pp. 1–4.
16. Mo, S.; Zhang, D.; Li, Z.; Wan, Z. The Possibility of Fault Location in Cross-Bonded Cables by Broadband Impedance Spectroscopy. *IEEE Trans. Dielectr. Electr. Insul.* **2021**, *28*, 1416–1423. [CrossRef]
17. Wang, S.; Liu, J.; Huang, J.; Zhang, H.; Li, Z.; Cao, J. A cascaded high-voltage high-frequency linear amplifier for power transmission line measurement. *Measurement* **2024**, *227*, 114255. [CrossRef]

18. Zhou, Z.; Zhang, D.; He, J.; Li, M. Local Degradation Diagnosis for Cable Insulation based on Broadband Impedance Spectroscopy. *IEEE Trans. Dielectr. Electr. Insul.* **2015**, *22*, 2097–2107. [CrossRef]
19. Yang, Y.; Hepburn, D.M.; Zhou, C.; Zhou, W.; Bao, Y. On-line Monitoring of Relative Dielectric Losses in Cross-bonded Cables Using Sheath Currents. *IEEE Trans. Dielectr. Electr. Insul.* **2017**, *24*, 2677–2685. [CrossRef]
20. Hua, X.; Wang, L.; Yang, S. Multiscale Analysis of the Aging Process of Cable Insulation. *IEEE Trans. Dielectr. Electr. Insul.* **2022**, *30*, 238–246. [CrossRef]
21. Wang, Q.; Liu, R.; Qin, S.; Chen, X.; Shen, Z.; Hou, Z. Insulation Properties and Degradation Mechanism for XLPE Subjected to Different Aging Periods. *CSEE J. Power Energy Syst.* **2023**, *9*, 1959–1967. [CrossRef]
22. Zhang, Q.; Li, K.; Chen, L.; Luo, J.; Zhao, Z. Identification and Localization Study of Grounding System Defects in Cross-Bonded Cables. *Electronics* **2025**, *14*, 622. [CrossRef]
23. Chi, P.; Qin, Y.; Tao, Y.; Liang, R. Research on condition assessment of XLPE cable based on signal propagation characteristics. *Electr. Power Syst. Res.* **2021**, *195*, 107136. [CrossRef]

Disclaimer/Publisher's Note: The statements, opinions and data contained in all publications are solely those of the individual author(s) and contributor(s) and not of MDPI and/or the editor(s). MDPI and/or the editor(s) disclaim responsibility for any injury to people or property resulting from any ideas, methods, instructions or products referred to in the content.